



Swansea University  
Prifysgol Abertawe



## Cronfa - Swansea University Open Access Repository

---

This is an author produced version of a paper published in :  
*Journal of Intelligent Material Systems and Structures*

Cronfa URL for this paper:

<http://cronfa.swan.ac.uk/Record/cronfa33943>

---

### Paper:

Mousavi Lajimi, S. & Friswell, M. (2017). Energy harvesting from a non-linear standing beam–mass system: Two-versus one-mode approximations. *Journal of Intelligent Material Systems and Structures*, 28(8), 1010-1022.  
<http://dx.doi.org/10.1177/1045389X16667852>

---

This article is brought to you by Swansea University. Any person downloading material is agreeing to abide by the terms of the repository licence. Authors are personally responsible for adhering to publisher restrictions or conditions. When uploading content they are required to comply with their publisher agreement and the SHERPA RoMEO database to judge whether or not it is copyright safe to add this version of the paper to this repository.

<http://www.swansea.ac.uk/iss/researchsupport/cronfa-support/>

---

# Energy harvesting from a non-linear standing beam-mass system: two-versus one-mode approximations

Journal Title  
XX(X):1-10  
© The Author(s) 2015  
Reprints and permission:  
sagepub.co.uk/journalsPermissions.nav  
DOI: 10.1177/ToBeAssigned  
www.sagepub.com/



S. Amir Mousavi Lajimi<sup>1</sup> and Michael I. Friswell<sup>2</sup>

## Abstract

We investigate the effect of including the second mode of natural vibration on the computed response of a forced nonlinear gravity-loaded beam-mass structure used for non-linear piezoelectric energy harvesting. By using the method of assumed-modes and Lagrange equations, we develop the discretized equations of generalized coordinates of the system including the electro-mechanical equation. The equation of motion is further simplified to find the single-mode approximation. The phase-portraits, time-histories, Poincaré sections, and frequency-response curves of the system are computed. It is shown that the number of mode-shapes affects the response and it is required to include higher modes to improve the analytical-computational results. The system shows distinct behavior varying from a linear single-frequency response to a multi-frequency chaotic response. The average power across the load resistor consequently shows a noticeable variation depending on the characteristics of the overall system response.

## Keywords

energy harvesting, piezoelectric, bi-stable, non-linear dynamics

## Introduction

Ideally environmental energy harvesting is combined with wire-less technologies to produce self-powered devices (Paradiso et al. 2005). As a result, either the energy is directly used by the device or used to re-charge the battery for future usage. Ordinarily, linear direct resonance has been the fundamental method for environmental energy harvesting (Priya and Inman 2009). To this end, the energy harvesting system must be designed such that its resonance frequency matches closely the environmentally induced excitation, obviously placing restrictions on the device performance and usefulness. Technically speaking, a linear system under resonance would have a limited bandwidth and may not generate a high power unless excited near the resonance frequency or by a high amplitude excitation.

Various methods and mechanisms have been introduced to remove the limitations associated with linear energy harvesting. One approach is to integrate several cantilevers into the system to optimize the harvesting system. Ferrari et al. (2008) used several cantilevers with different lengths to widen the harvesting spectrum for a battery-less sensor package. Similarly, to create a multi-frequency spectra Xue et al. (2008) employed an array of piezoelectric bimorphs harvesters connected either in parallel or in series. Another possibility to widen the peak-performance area, is to use

nonlinear energy harvesting methods (Cottone et al. 2009; Mann and Sims 2009). Essentially based on the bi-stable system of Moon and Holmes (1979), many harvesters have been designed and used to rectify issues associated with linear harvesters, e.g. Stanton et al. (2009); Erturk and Inman (2011). A brief review of the use of bi-stability for energy harvesting is given by Harne and Wang (2013).

To realise a bi-stable energy harvester, Friswell et al. (2012) proposed a standing beam carrying an end mass. The end (tip) mass induced axial load may be chosen to force the structure into a post-buckled configuration where two stable equilibrium points exist. The beam may oscillate around the stable undeformed position before buckling or around either of two stable non-zero equilibrium states after buckling. It may also settle to a large stable orbit visiting both equilibrium points during each period. The system provides an opportunity to harvest energy from low frequencies. The single-degree-of-freedom model proposed

---

<sup>1</sup> Systems Design Engineering Alumni, University of Waterloo, Canada

<sup>2</sup> College of Engineering, Swansea University, UK

## Corresponding author:

S. Amir Mousavi Lajimi, University of Waterloo, N2L 1W2, Canada  
Email: samousav@uwaterloo.ca

by Friswell et al. (2012) suffers from inaccurate estimation of the response compared with the experimental results.

In this paper we choose a different approach and develop both one- and two-degree-of-freedom models of the standing beam-mass system. We investigate the effect of the second mode on the system response and demonstrate how the predictions differ from the single-mode approximation. The effects of the higher mode on the response and the average harvested power are examined by computing the time-histories, Poincaré section, bifurcation diagram, and frequency response curves. It is shown that the higher mode may need to be included to compute the system output for certain system parameters but not for all of them.

## Mathematical model of the system

The schematic of the energy harvesting system is shown in Figure 1 including the standing uniform beam carrying an end-mass. In practice, the piezo patch, not shown in the picture, is attached to the beam near its clamped end. For the structure under investigation the main parameter values are listed in Table 1. For this study, the tip-mass is varied in the range 0g to 16g, and the beam's effective length is fixed at 275mm. The piezo-electric patch can be added to the beam in either unimorph or bimorph configurations by changing the piezo-electric constant appearing in the moment equation (Crawley and De Luis 1987; Park et al. 1996). For this analysis, the piezocomposite patch operates in the unimorph 31-mode configuration to maximize the power output (Friswell et al. 2012). Therefore, the induced moment by a voltage  $V(t)$  across the piezoelectric layers is written as

$$M_c(s, t) = \Upsilon_c V(t) \quad (1)$$

where for a unimorph piezoelectric patch

$$\Upsilon_c = E_c d_{31} b_c \left( h + \frac{h_c}{2} - \bar{z} \right) \quad (2)$$

and  $h$  is the beam's thickness,  $h_c$  is the piezo's thickness,  $b_c$  is the piezo's width, and  $\bar{z}$  is the effective neutral axis (Park et al. 1996).

The kinetic energy is expressed in the form

$$\begin{aligned} \mathcal{K} = & \frac{1}{2} \rho A \int_0^L \left( \frac{\partial}{\partial t} v_p(s, t) + \frac{d}{dt} z(t) \right)^2 + \left( \frac{\partial}{\partial t} u_p(s, t) \right)^2 ds \\ & + \frac{1}{2} M \left( \left( \frac{d}{dt} v(t) + \frac{d}{dt} z(t) \right)^2 + \left( \frac{d}{dt} u(t) \right)^2 \right) \\ & + \frac{1}{2} J \left( \frac{d}{dt} \phi(t) \right)^2 \end{aligned} \quad (3)$$

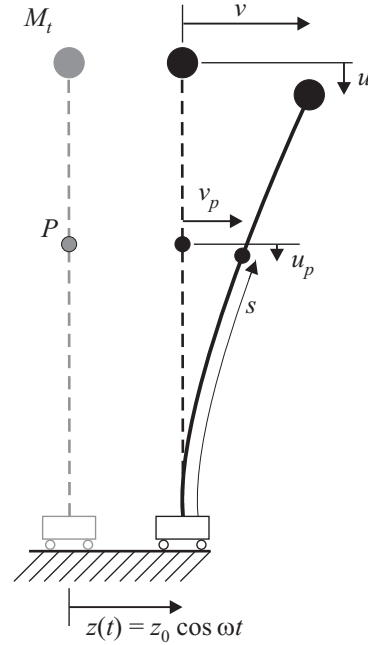


**Figure 1.** The schematic of the cantilever-mass system with horizontal base-excitation. The figure is not drawn to scale.

and the potential energy in the form

$$\mathcal{P} = \frac{1}{2} EI \int_0^L \kappa(s, t)^2 ds - \rho A g \int_0^L u_p(s, t) ds - M g u(t) \quad (4)$$

where the curvature is computed by the following approximation

$$\kappa(s, t) \approx \frac{\partial^2}{\partial s^2} v_p(s, t) \left( 1 + \frac{1}{2} \left( \frac{\partial}{\partial s} v_p(s, t) \right)^2 \right) \quad (5)$$

and the slope is computed from (Friswell et al. 2012)

$$\begin{aligned} \phi_p(s, t) &= \arcsin \left( \frac{\partial}{\partial s} v_p(s, t) \right) \\ &\approx \frac{\partial}{\partial s} v_p(s, t) + \frac{1}{6} \left( \frac{\partial}{\partial s} v_p(s, t) \right)^3. \end{aligned} \quad (6)$$

The work done by the piezoelectric patch is given by

$$W = \int_0^{L_c} M_\Lambda(s, t) \kappa(s, t) ds \quad (7)$$

where  $L_c$  is the active length of the patch attached near the beam's clamped-end. Substituting equation (1) into equation (7) and employing equation (2), we find the final form of the work done by the piezo. The axial displacement relates to the transverse deflection through the

in-extensibility condition given by

$$u_p(s, t) = \frac{1}{2} \int_0^s \left( \frac{\partial}{\partial \xi} v_p(\xi, t) \right)^2 d\xi \quad (8)$$

The multi-mode approximation of the response is

$$v(s, t) = \sum_{n=1}^N \psi_n(s) q_n(t) \quad (9)$$

where  $N$  indicates the number of linear modes,  $\psi_n(s)$ , which are obtained by solving the linear eigenvalue problem for a simple clamped-free beam with the same dimensions as in Table 1. Of course the response of the beam will be non-linear and these linear modes do not represent the actual response of the system. However the linear modes define a subspace onto which the non-linear response is projected; if sufficient linear modes are retained then the reduced order model will capture the dynamics of the full non-linear model.

Inserting equation (9) into equations (3)-(8) and substituting the discretized kinetic and potential energies and the piezo work into Lagrange's equations results in the following two-degree-of-freedom model including the harvesting circuit equation:

$$\begin{aligned} & \left( \Phi_1 q_1^2 + 2\Phi_2 q_2 q_1 + \Phi_3 q_2^2 + \Phi_4 \right) \dot{q}_1 + (\Phi_1 q_1 + \Phi_2 q_2) \dot{q}_1^2 \\ & + \left( \Phi_{14} q_2^2 + \Phi_{15} \right) q_1 + \Phi_{11} q_1^3 + \Phi_{12} q_2 q_1^2 - \Phi_{16} q_2 \\ & + \left( \Phi_5 q_1^2 + \Phi_6 q_2 q_1 + \Phi_7 q_2^2 + \Phi_8 \right) \dot{q}_2 + \Phi_{13} q_2^3 \\ & + (2\Phi_2 q_1 + 2\Phi_3 q_2) \dot{q}_2 \dot{q}_1 + (\Phi_9 q_1 + \Phi_{10} q_2) \dot{q}_2^2 \\ & + \Upsilon_c \left( \frac{3}{2} \sigma_2 q_1^2 + \sigma_4 q_2 q_1 + 2\sigma_5 q_2 q_1 + \sigma_6 q_2^2 \right. \\ & \quad \left. + \frac{1}{2} \sigma_7 q_2^2 + \sigma_1 \right) V(t) = -\Phi_{17} \ddot{z} \quad (10) \end{aligned}$$

$$\begin{aligned} & \left( \Psi_1 q_1^2 + 2\Psi_2 q_2 q_1 + \Psi_3 q_2^2 + \Psi_4 \right) \dot{q}_2 + (\Psi_3 q_2 + \Psi_2 q_1) \dot{q}_2^2 \\ & + \left( \Psi_{13} q_1^2 - \Psi_{14} \right) q_2 + \Psi_{11} q_2^3 + \Psi_{12} q_1 q_2^2 - \Psi_{16} q_1 \\ & + \left( \Psi_5 q_1^2 + \Psi_6 q_2 q_1 + \Psi_7 q_2^2 + \Psi_8 \right) \dot{q}_1 + \Psi_{15} q_1^3 \\ & + (2\Psi_4 q_2 + 2\Psi_1 q_1) \dot{q}_1 \dot{q}_2 + (\Psi_9 q_2 + \Psi_{10} q_1) \dot{q}_1^2 \\ & + \Upsilon_c \left( \frac{3}{2} \sigma_8 q_2^2 + 2\sigma_6 q_2 q_1 + \sigma_7 q_2 q_1 + \sigma_3 \right. \\ & \quad \left. + \frac{1}{2} \sigma_4 q_1^2 + \sigma_5 q_1^2 \right) V(t) = \Psi_{17} \ddot{z}, \quad (11) \end{aligned}$$

$$\begin{aligned} & \Upsilon_c \left( \left( \frac{3}{2} \sigma_2 q_1^2 + \sigma_4 q_2 q_1 + 2\sigma_5 q_2 q_1 + \sigma_6 q_2^2 \right. \right. \\ & \quad \left. \left. + \frac{1}{2} \sigma_7 q_2^2 + \sigma_1 \right) \dot{q}_1 + \left( \frac{3}{2} \sigma_8 q_2^2 + 2\sigma_6 q_2 q_1 \right. \right. \end{aligned}$$

$$\begin{aligned} & \left. + \sigma_7 q_2 q_1 + \frac{1}{2} \sigma_4 q_1^2 + \sigma_5 q_1^2 + \sigma_3 \right) \dot{q}_2 \Big) \\ & + C_p \dot{V} + \frac{V}{R_l} = 0 \quad (12) \end{aligned}$$

where

$$\Phi_1 = \rho A \gamma_6 + J \beta_1 \beta_2 + M \alpha_1(L)^2 \quad (13)$$

$$\Phi_2 = \rho A \gamma_7 + J \beta_1 \beta_3 + M \alpha_1(L) \alpha_2(L) \quad (14)$$

$$\Phi_3 = \rho A \gamma_9 + J \beta_1 \beta_4 + M \alpha_2(L)^2 \quad (15)$$

$$\Phi_4 = \rho A \gamma_3 + J \beta_1^2 + M \psi_1(L)^2 \quad (16)$$

$$\Phi_5 = \rho A \gamma_7 + \frac{1}{2} J (\beta_1 \beta_3 + \beta_2 \beta_5) + M \alpha_1(L) \alpha_2(L) \quad (17)$$

$$\begin{aligned} \Phi_6 = & \rho A (\gamma_8 + \gamma_9) + J (\beta_1 \beta_4 + \beta_3 \beta_5) \\ & + M \left( \alpha_2(L)^2 + \alpha_1(L) \alpha_3(L) \right) \quad (18) \end{aligned}$$

$$\Phi_7 = \rho A \gamma_{10} + \frac{1}{2} J (\beta_4 \beta_5 + \beta_1 \beta_6) + M \alpha_2(L) \alpha_3(L) \quad (19)$$

$$\Phi_8 = \rho A \gamma_4 + J \beta_1 \beta_5 + M \psi_1(L) \psi_2(L) \quad (20)$$

$$\Phi_9 = \rho A \gamma_8 + J \beta_1 \beta_4 + M \alpha_1(L) \alpha_3(L) \quad (21)$$

$$\Phi_{10} = \rho A \gamma_{10} + J \beta_1 \beta_6 + M \alpha_2(L) \alpha_3(L) \quad (22)$$

$$\Phi_{11} = 2EI \Gamma_4 \quad (23)$$

$$\Phi_{12} = 3EI (\Gamma_5 + \Gamma_7) \quad (24)$$

$$\Phi_{13} = EI (\Gamma_9 + \Gamma_{11}) \quad (25)$$

$$\Phi_{14} = EI (\Gamma_6 + 4\Gamma_8 + \Gamma_{10}) \quad (26)$$

$$\Phi_{15} = EI \Gamma_1 - \rho A g \gamma_{12} - M g \alpha_1(L) \quad (27)$$

$$\Phi_{16} = \rho A g \gamma_{13} - EI \Gamma_2 + M g \alpha_2(L) \quad (28)$$

$$\Phi_{17} = \rho A \gamma_1 + M \psi_1(L) \quad (29)$$

and

$$\Psi_1 = \rho A \gamma_9 + J \beta_3 \beta_5 + M \alpha_2(L)^2 \quad (30)$$

$$\Psi_2 = \rho A \gamma_{10} + J \beta_4 \beta_5 + M \alpha_2(L) \alpha_3(L) \quad (31)$$

$$\Psi_3 = \rho A \gamma_{11} + J \beta_5 \beta_6 + M \alpha_3(L)^2 \quad (32)$$

$$\Psi_4 = \rho A \gamma_5 + J \beta_5^2 + M \psi_2(L)^2 \quad (33)$$

$$\begin{aligned} \Psi_5 = & \rho A \gamma_7 + \frac{1}{2} J (\beta(L)_1 \beta(L)_3 + \beta_2 \beta_5) \\ & + M \alpha_1(L) \alpha_2(L) \quad (34) \end{aligned}$$

$$\begin{aligned} \Psi_6 = & \rho A (\gamma_8 + \gamma_9) + J (\beta_1 \beta_4 + \beta_3 \beta_5) \\ & + M \left( \alpha_2(L)^2 + \alpha_1(L) \alpha_3(L) \right) \quad (35) \end{aligned}$$

$$\Psi_7 = \rho A \gamma_{10} + \frac{1}{2} J (\beta_4 \beta_5 + \beta_1 \beta_6) + M \alpha_2(L) \alpha_3(L) \quad (36)$$

$$\Psi_8 = \rho A \gamma_4 + J \beta_1 \beta_5 + M \psi_1(L) \psi_2(L) \quad (37)$$

$$\Psi_9 = \rho A \gamma_8 + J \beta_3 \beta_5 + M \alpha_1(L) \alpha_3(L) \quad (38)$$

$$\Psi_{10} = \rho A \gamma_7 + J \beta_2 \beta_5 + M \alpha_1(L) \alpha_2(L) \quad (39)$$

$$\Psi_{11} = 2EI \Gamma_{12} \quad (40)$$

$$\Psi_{12} = 3EI (\Gamma_9 + \Gamma_{11}) \quad (41)$$

$$\Psi_{13} = EI (\Gamma_6 + 4\Gamma_8 + \Gamma_{10}) \quad (42)$$

$$\Psi_{14} = \rho A g \gamma_{14} - EI \Gamma_3 + M g \alpha_3(L) \quad (43)$$

$$\Psi_{15} = EI (\Gamma_5 + \Gamma_7) \quad (44)$$

$$\Psi_{16} = \rho A g \gamma_{13} - EI \Gamma_2^2 + M g \alpha_2(L) \quad (45)$$

$$\Psi_{17} = \rho A \gamma_2 + M \psi_2(L) \quad (46)$$

$$\Gamma_1 = \int_0^L \psi_1''(s)^2 ds,$$

$$\Gamma_2 = \int_0^L \psi_1''(s) \psi_2''(s) ds,$$

$$\Gamma_3 = \int_0^L \psi_2''(s)^2 ds,$$

$$\Gamma_4 = \int_0^L (\psi_1'(s) \psi_1''(s))^2 ds,$$

$$\Gamma_5 = \int_0^L \psi_1'(s)^2 \psi_1''(s) \psi_2''(s) ds,$$

$$\Gamma_6 = \int_0^L (\psi_1'(s) \psi_2''(s))^2 ds,$$

$$\Gamma_7 = \int_0^L \psi_1'(s) \psi_2'(s) \psi_1''(s)^2 ds,$$

$$\Gamma_8 = \int_0^L \psi_1'(s) \psi_2'(s) \psi_1''(s) \psi_2''(s) ds,$$

$$\Gamma_9 = \int_0^L \psi_1'(s) \psi_2'(s) \psi_2''(s)^2 ds,$$

$$\Gamma_{10} = \int_0^L (\psi_2'(s) \psi_1''(s))^2 ds,$$

$$\Gamma_{11} = \int_0^L \psi_2'(s)^2 \psi_1''(s) \psi_2''(s) ds,$$

$$\Gamma_{12} = \int_0^L (\psi_2'(s) \psi_2''(s))^2 ds,$$

$$\Gamma_{13} = \int_0^L \psi_1'(s)^4 \psi_1''(s)^2 ds,$$

$$\Gamma_{14} = \int_0^L \psi_1'(s)^4 \psi_1''(s) \psi_2''(s) ds,$$

$$\Gamma_{15} = \int_0^L \psi_1'(s)^4 \psi_2''(s)^2 ds,$$

$$\Gamma_{16} = \int_0^L \psi_1'(s)^3 \psi_2'(s) \psi_1''(s)^2 ds,$$

$$\Gamma_{17} = \int_0^L \psi_1'(s)^3 \psi_2'(s) \psi_1''(s) \psi_2''(s) ds,$$

$$\Gamma_{18} = \int_0^L \psi_1'(s)^3 \psi_2'(s) \psi_2''(s)^2 ds,$$

$$\Gamma_{19} = \int_0^L (\psi_1'(s) \psi_2'(s) \psi_1''(s))^2 ds,$$

$$\Gamma_{20} = \int_0^L (\psi_1'(s) \psi_2'(s))^2 \psi_1''(s) \psi_2''(s) ds,$$

$$\Gamma_{21} = \int_0^L (\psi_1'(s) \psi_2'(s) \psi_2''(s))^2 ds,$$

$$\Gamma_{22} = \int_0^L \psi_1'(s) \psi_2'(s)^3 \psi_1''(s)^2 ds,$$

$$\Gamma_{23} = \int_0^L \psi_1'(s) \psi_2'(s)^3 \psi_1''(s) \psi_2''(s) ds,$$

$$\Gamma_{24} = \int_0^L \psi_1'(s) \psi_2'(s)^3 \psi_2''(s)^2 ds,$$

$$\Gamma_{25} = \int_0^L \psi_2'(s)^4 \psi_1''(s)^2 ds,$$

$$\Gamma_{26} = \int_0^L \psi_2'(s)^4 \psi_1''(s) \psi_2''(s) ds,$$

$$\Gamma_{27} = \int_0^L \psi_2'(s)^4 \psi_2''(s)^2 ds \quad (47)$$

$$\gamma_1 = \int_0^L \psi_1(s) ds, \quad \gamma_2 = \int_0^L \psi_2(s) ds,$$

$$\gamma_3 = \int_0^L \psi_1(s)^2 ds, \quad \gamma_4 = \int_0^L \psi_1(s) \psi_2(s) ds,$$

$$\gamma_5 = \int_0^L \psi_2(s)^2 ds, \quad \gamma_6 = \int_0^L \alpha_1(s)^2 ds,$$

$$\gamma_7 = \int_0^L \alpha_1(s) \alpha_2(s) ds, \quad \gamma_8 = \int_0^L \alpha_1(s) \alpha_3(s) ds,$$

$$\gamma_9 = \int_0^L \alpha_2(s)^2 ds, \quad \gamma_{10} = \int_0^L \alpha_2(s) \alpha_3(s) ds,$$

$$\gamma_{11} = \int_0^L \alpha_3(s)^2 ds, \quad \gamma_{12} = \int_0^L \alpha_1(s) ds,$$

$$\gamma_{13} = \int_0^L \alpha_2(s) ds, \quad \gamma_{14} = \int_0^L \alpha_3(s) ds \quad (48)$$

$$\beta_1 = \psi_1'(L), \quad \beta_2 = \psi_1'(L)^3, \quad \beta_3 = \psi_1'(L)^2 \psi_2'(L), \\ \beta_4 = \psi_1'(L) \psi_2'(L)^2, \quad \beta_5 = \psi_2'(L), \quad \beta_6 = \psi_2'(L)^3 \quad (49)$$

and

$$\alpha_1(s) = \int_0^s \psi_1'(\xi)^2 d\xi, \quad \alpha_2(s) = \int_0^s \psi_1'(\xi) \psi_2'(\xi) d\xi, \\ \alpha_3(s) = \int_0^s \psi_2'(\xi)^2 d\xi \quad (50)$$

**Table 1.** System specifications

Structure					
$L$	$h$	$b$	$E$	$\rho$	
275 mm	0.245 mm	15.88 mm	210 GPa	7850 kg/m <sup>3</sup>	
Piezo harvester					
$L_c$	$b_c$	$h_c$	$C_p$	$R_l$	
28 mm	14 mm	300 $\mu$ m	25.7 nF	9.944 M $\Omega$	

The average power scavenged between times  $T_1$  and  $T_2$  is computed as  $P_{ave} = \frac{1}{T_2 - T_1} \int_{T_1}^{T_2} \frac{V(t)^2}{R_l} dt$ .

The coefficients of equations (10) to (12) are evaluated using the mode-shapes of the cantilever beam given by

$$\psi_n = c_n \left( \frac{\sin(\lambda L) - \sinh(\lambda L)}{\cosh(\lambda L) + \cos(\lambda L)} (\sinh(\lambda s) - \sin(\lambda s)) + \cosh(\lambda s) - \cos(\lambda s) \right) \quad (51)$$

where the  $\lambda$ 's are the eigenvalues of the cantilever beam found by computing the roots of  $1 + \cos(\lambda L) \cosh(\lambda L) = 0$  and  $c_n$  normalizes the eigenfunctions such that  $\rho A \int_0^L \psi_n(\xi)^2 d\xi = 1$ . For a one-degree-of-freedom model we set  $\dot{q}_2 = 0, \ddot{q}_2 = 0, q_2 = 0$  in equation (10) and obtain

$$\left( \Phi_1 q_1^2 + \Phi_4 \right) \ddot{q}_1 + \Phi_1 q_1 \dot{q}_1^2 + \Phi_{11} q_1^3 + \Phi_{15} q_1 + \Upsilon_c V(t) \left( \frac{3}{2} \sigma_2 q_1^2 + \sigma_1 \right) = -\Phi_{17} \ddot{z} \quad (52)$$

## Computational analysis of the system

The standing beam may buckle under the load of the end mass and oscillate between two deformed equilibrium positions. To obtain the non-zero equilibrium positions, we set  $\ddot{q}_1 = 0, \dot{q}_1 = 0, \ddot{q}_2 = 0, \dot{q}_2 = 0$ , and  $\ddot{z} = 0$  in equations (10) and (11), and solve for  $q_1$  and  $q_2$  and find the static equilibrium positions from equation (9). Figure 2 shows the equilibrium positions as the tip-mass is increased from 0 to 15 g for the harvester with parameters listed in Table 1. The undeformed equilibrium position loses its stability at 11.3 g. Upon buckling two stable equilibrium positions appear on both sides the unstable upright position. Note that the beam response is non-linear even when the tip mass is insufficient to cause buckling.

### Time-histories and Poincaré section

The response of the beam harvester, whose parameters are listed in Table 1, is computed for an excitation frequency of 0.4 Hz and amplitude  $z_0 = 15$  mm, for the two mode approximation. The load resistance is fixed at 9.944 M $\Omega$ ,

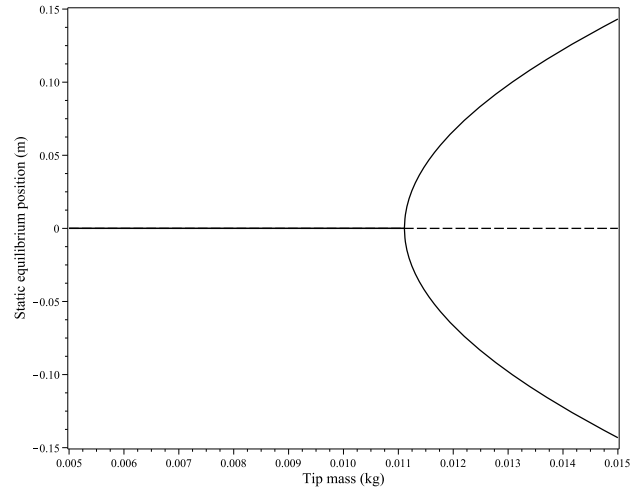


**Figure 2.** Static equilibrium positions (two-mode approximation) for varying tip mass.

which is close to the optimum given by Friswell et al. (2012). The response for six tip masses are considered that show a variety of dynamic response. The time response is computed for 6000 cycles and the last 40 cycles are shown in Figure 3, where the response has settled in the steady state. Periodic solutions occur for small tip masses ( $M = 10$  g and  $M = 10.5$  g) where the beam oscillates around its central equilibrium position. Periodic solutions also occur for large tip masses ( $M = 14$  g and  $M = 16$  g), but now the oscillation occurs about one of the buckled equilibrium positions; the initial conditions will determine which of the two equilibrium positions is chosen. For tip masses close to the critical value for buckling ( $M = 11.4$  g and  $M = 13.1$  g) the response is non-periodic. For the tip mass  $M = 13.1$  g enough energy is injected into the system to oscillate between the two equilibrium positions for the buckled beam. Figure 4 shows the phase-portraits and highlights that the periodic solutions are not necessarily harmonic and emphasises that the response is non-linear even before the beam buckles. The non-periodic response is clearly chaotic. Figure 5 shows the corresponding voltage for the different tip masses, which follows the beam response closely.

The end mass plays the role of a bifurcation parameter and changes the system behavior, as shown in Figure 6. The bifurcation diagram is generated by sampling the response for 100 cycles after simulating for 6000 cycles to allow the transients to decay. The base excitation amplitude is  $z = 15$  mm. The mass is varied from 8 g to 16 g in steps of 0.1 g; higher resolutions would provide a better understanding of the system response but require access to powerful computational resources. Regions of periodic responses and chaos are identified in the bifurcation diagram. In particular the response for low or high mass values has the same

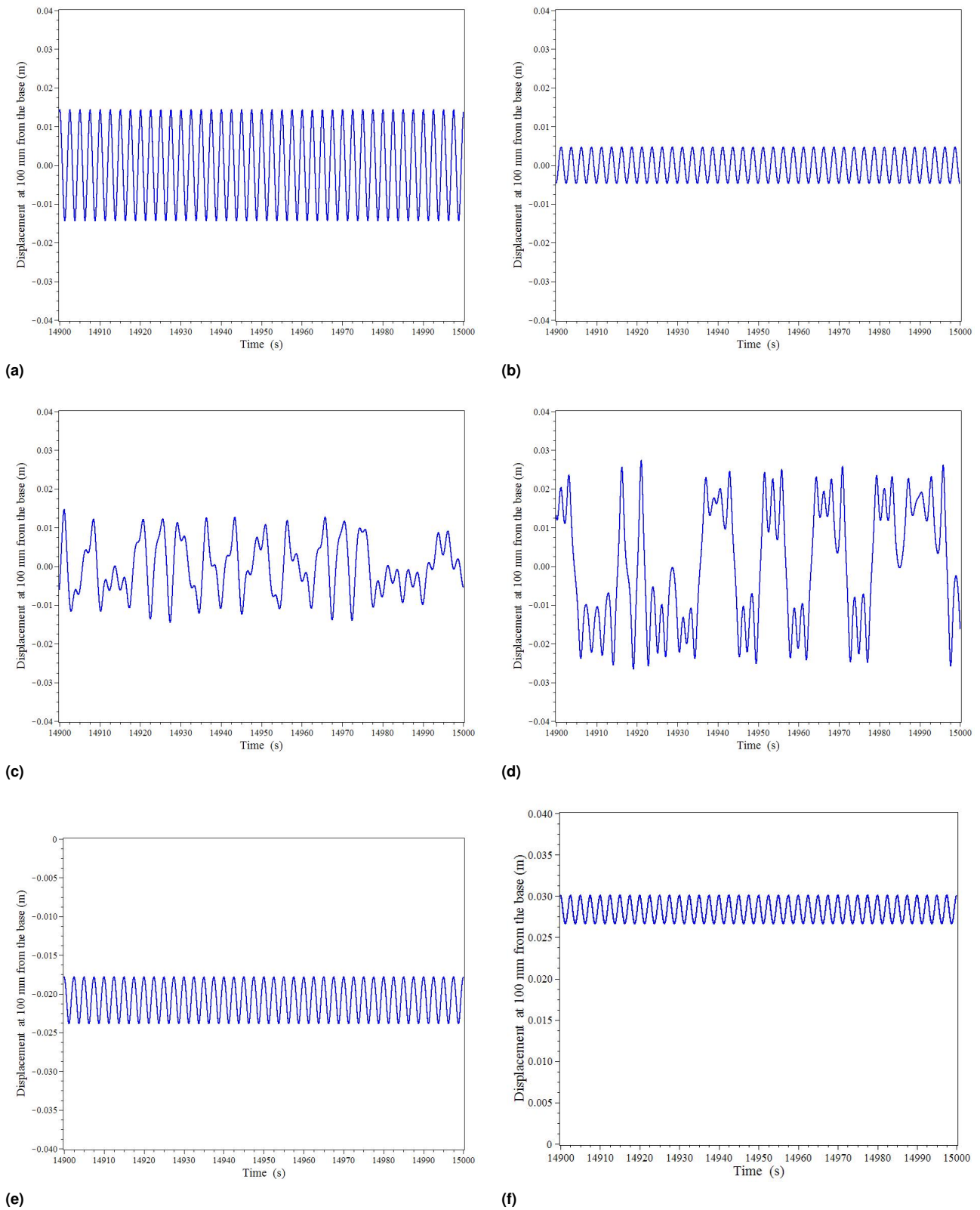


**Figure 3.** The steady state displacement at 100mm from the base with  $z_0 = 15\text{mm}$ : (a)  $M = 10\text{ g}$ , (b)  $M = 10.5\text{ g}$  (c)  $M = 11.4\text{ g}$  (d)  $M = 13.1\text{ g}$  (e)  $M = 14\text{ g}$  (f)  $M = 16\text{ g}$ .

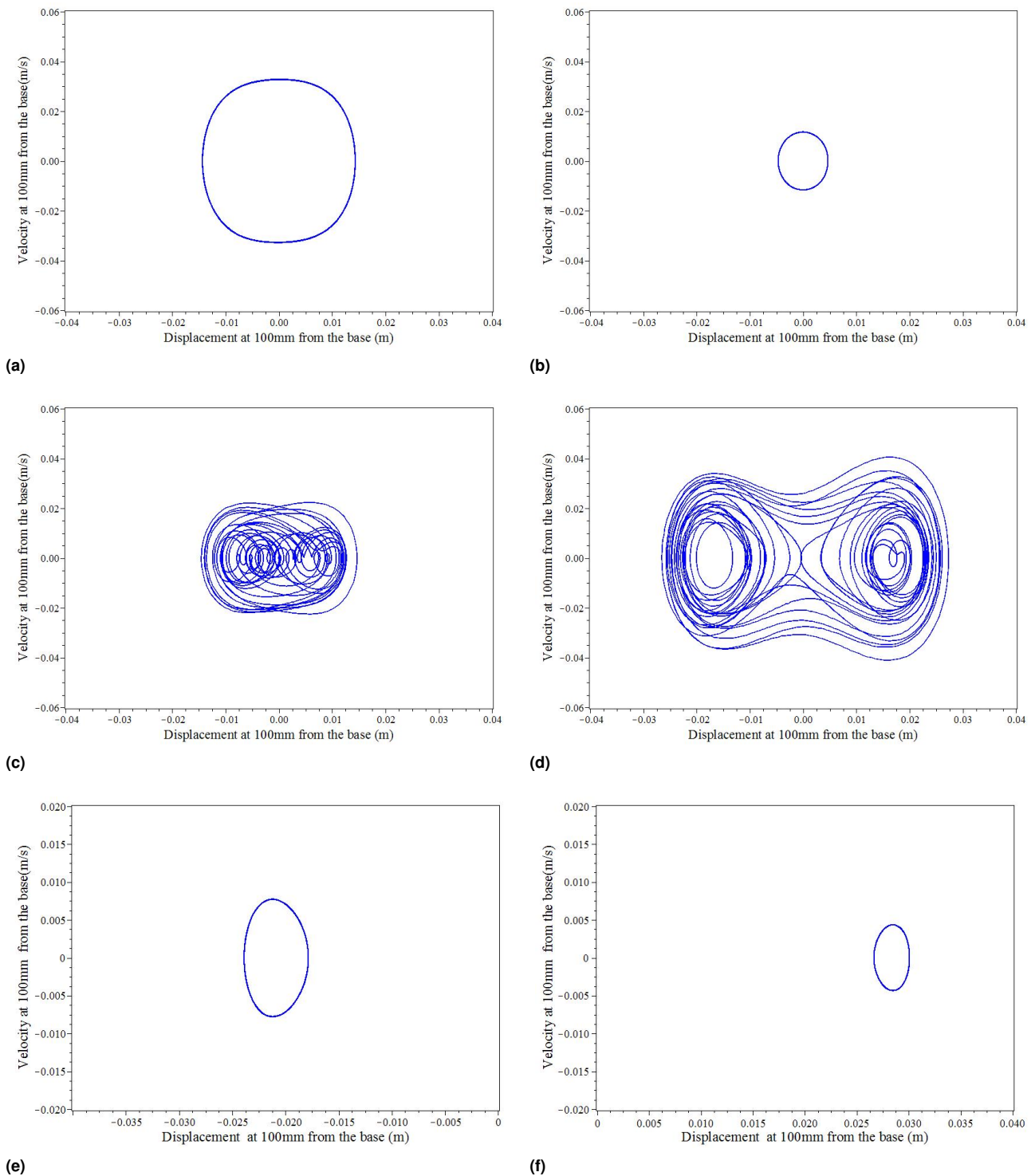


**Figure 4.** The phase-portrait at 100mm from the base with  $z_0 = 15\text{mm}$ : (a)  $M = 10\text{ g}$ , (b)  $M = 10.5\text{ g}$  (c)  $M = 11.4\text{ g}$  (d)  $M = 13.1\text{ g}$  (e)  $M = 14\text{ g}$  (f)  $M = 16\text{ g}$ .

period as the excitation. The phase and amplitude of this response changes significantly as the beam approaches the

critical tip mass for buckling. For high tip mass values the beam has buckled and the initial conditions determine

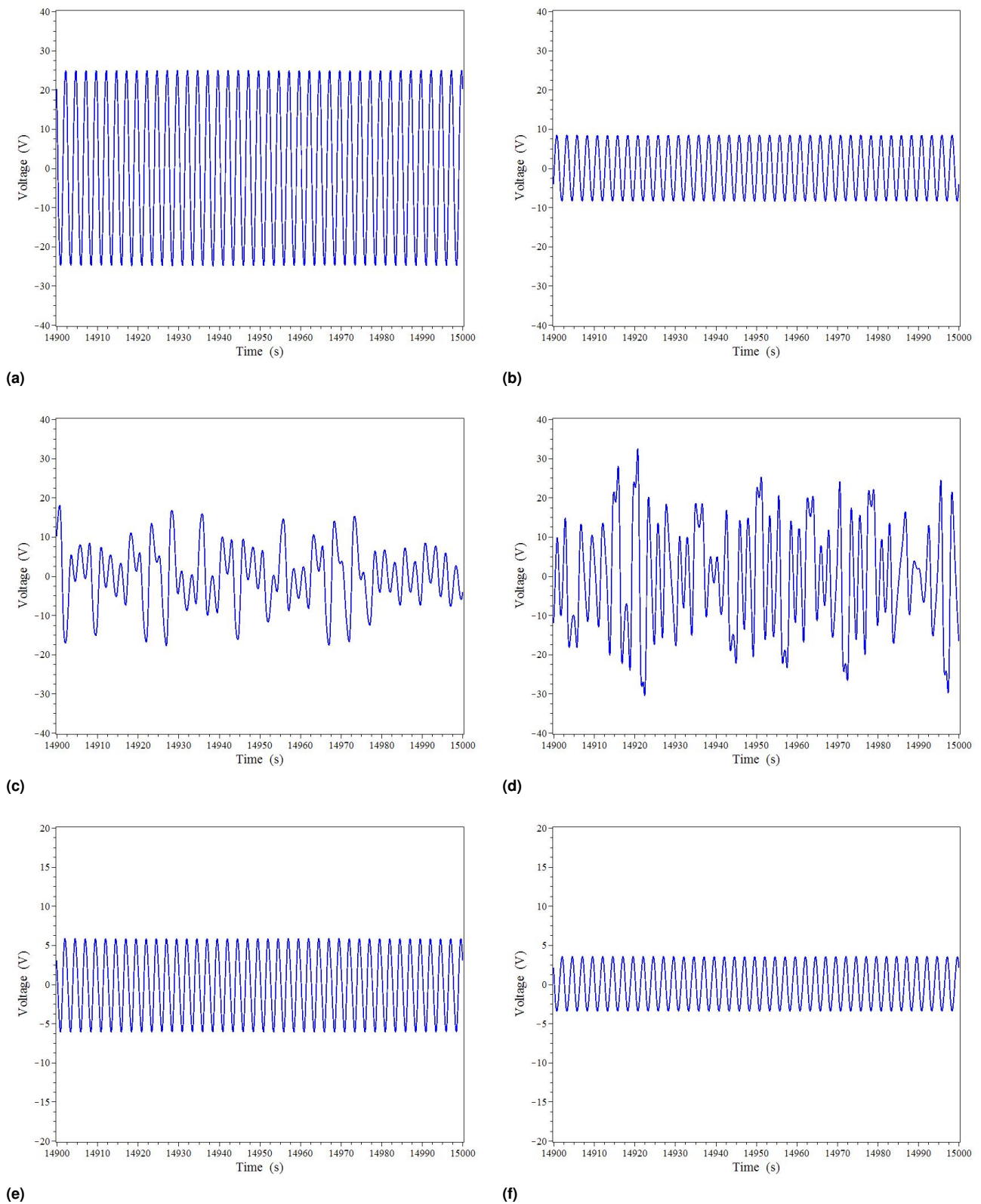


**Figure 5.** The voltage generated with  $z_0 = 15\text{mm}$ : (a)  $M = 10\text{ g}$ , (b)  $M = 10.5\text{ g}$  (c)  $M = 11.4\text{ g}$  (d)  $M = 13.1\text{ g}$  (e)  $M = 14\text{ g}$  (f)  $M = 16\text{ g}$ .

which equilibrium position the beam vibrates around. Figure 6b shows the average power generated for the different tip masses; the highest average power is generated just before the beam buckles.

One important question is the effect of the number of modeled modes on the response of the energy harvester. Figure 7 shows the displacement and average power bifurcation diagrams as the tip mass varies, for the same parameters as Figure 6. Although the character of the plots is similar there are a number of important differences. The single mode model is stiffer and hence the critical tip mass for buckling increases. Thus the maximum power occurs at a higher tip mass for the single mode model. Furthermore, the regions of chaos have moved to higher tip masses, and the region of periodic response around 12.5 to 13.5g has widened in the single mode model. The maximum predicted average power just before buckling has increased slightly for the single mode model, although for other tip mass values the predicted power is similar for both models.

### Frequency-response curves

The frequency-response curves provide us with significant information about the system response and bifurcation points. We investigate three cases where the end mass is removed, or is equal to 10.5 g or 14 g, and compute the response for a set of three excitation amplitudes: 5 mm, 10 mm, and 15 mm. The electrical resistance is set to 9.944 M $\Omega$  for all cases; the load resistance will not be the optimum for all excitation frequencies, but in practice it is very likely that the resistance would have to be fixed. The frequency response curves are computed by simulating a stepped sine test, where the frequency is first swept up, and then swept down. The beam displacement is non-dimensionalized with the maximum base displacement. The average harvested power is divided by the base acceleration squared; the result is not a non-dimensional quantity but does allow the different results to be plotted on the same axes.

Figure 8 shows the frequency response with no tip mass, and shows a response that is almost linear. However, some hardening behaviour is apparent as the resonant frequency increases with increasing base displacement. Note that the forward and backward sweeps of the excitation frequency give identical results. We further investigate the system near the buckling load and in the post-buckled state where we expect to see more significant differences in the system response. Figure 9 shows the response for  $M = 10.5$  g, which is just below the critical buckling mass. The response shows a hardening behavior for the system for larger excitation amplitudes, and the classical jump phenomena and multiple solutions are clearly apparent. Once the beam has buckled the response has a softening behavior, as shown

in Figure 10 for  $M = 14$  g. Jumps in the response are again clearly visible.

## Conclusion

The results of a computational study of a bistable nonlinear energy harvester depends on the discretized model of the system. A comparison with previous studies shows that the definition of the eigenfunction changes the response. The Poincaré section and bifurcation diagram indicate that the system may show chaotic response for certain set of parameters and excitation. For the pre-buckled configuration, the two-mode approximation of the response provides a more flexible system and a lower estimated average power than for the one-mode approximation. As the tip mass approaches the static bifurcation point where the upright position becomes unstable, the two- and one-mode approximations predict similar behavior, although at slightly different tip mass values. Given the results, further analytical, computational, and experimental investigations are required to reach a definite conclusion about the results and the effects of the higher modes.

The main purpose of this paper is reveal the parameters that affect the response of the beam harvester, and the quality of the model required to ensure accurate predictions of the system response and the resulting power. The harvester design would have to be optimised for a particular excitation force and energy requirements; this would determine some of the system parameters such as beam and piezoelectric dimensions. The non-linear response is significantly affected by the tip mass, and this could be tuned for particular situations, and also for compensate for variability in manufacture.

## References

- Cottone F, Vocca H and Gammaitoni L (2009) Nonlinear energy harvesting. *Physical Review Letters* 102(8): 080601.
- Crawley EF and De Luis J (1987) Use of piezoelectric actuators as elements of intelligent structures. *AIAA journal* 25(10): 1373–1385.
- Erturk A and Inman D (2011) Broadband piezoelectric power generation on high-energy orbits of the bistable duffing oscillator with electromechanical coupling. *Journal of Sound and Vibration* 330(10): 2339–2353.
- Ferrari M, Ferrari V, Guizzetti M, Marioli D and Taroni A (2008) Piezoelectric multifrequency energy converter for power harvesting in autonomous microsystems. *Sensors and Actuators A: Physical* 142(1): 329–335.
- Friswell MI, Ali SF, Bilgen O, Adhikari S, Lees AW and Litak G (2012) Non-linear piezoelectric vibration energy harvesting from a vertical cantilever beam with tip mass. *Journal of Intelligent Material Systems and Structures* 23(13): 1505–1521.

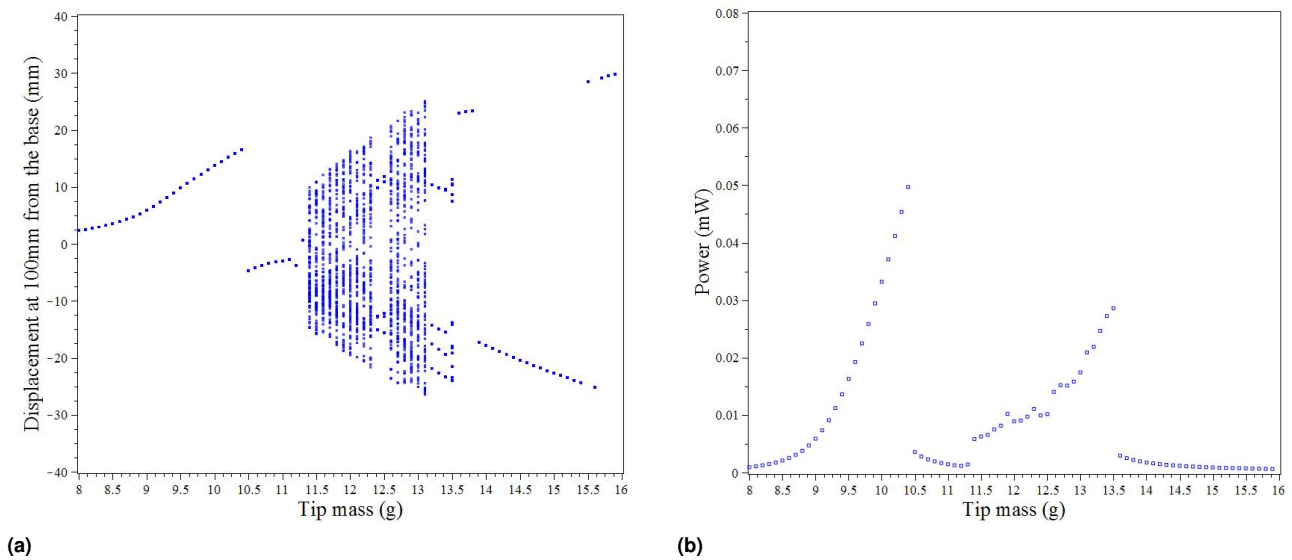


**Figure 6.** The bifurcation diagram (a) and average power (b) between 14900s and 15000s with  $z_0 = 15$ mm.

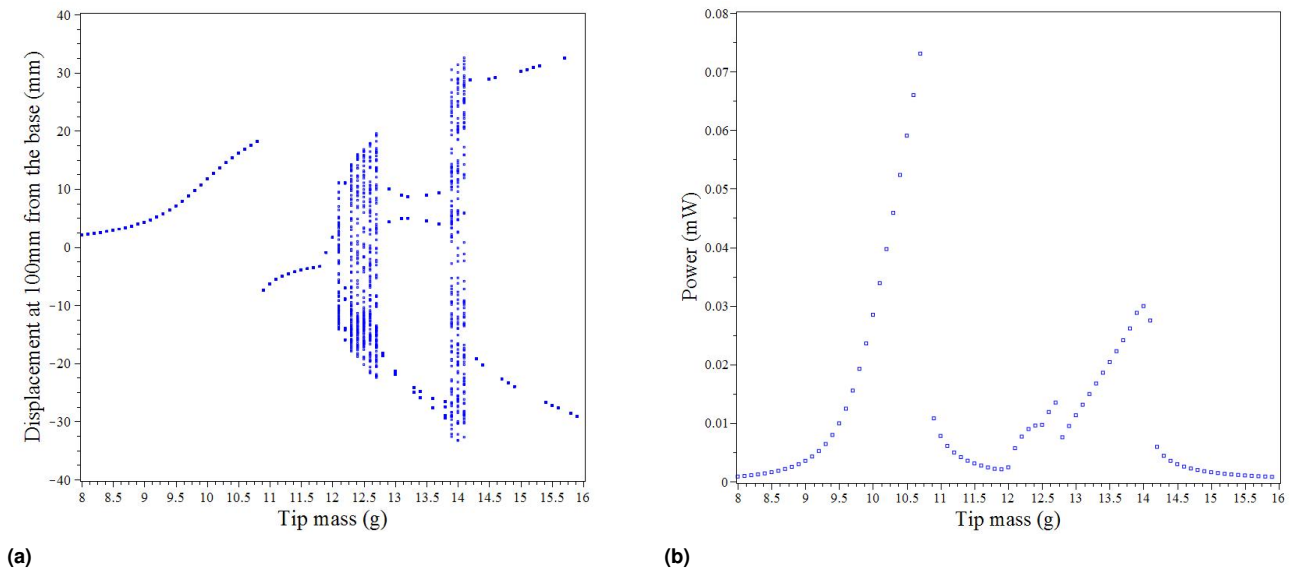


**Figure 7.** The bifurcation diagram (a) and average power (b) for the single mode approximation between 14900s and 15000s with  $z_0 = 15$ mm.

Harne R and Wang K (2013) A review of the recent research on vibration energy harvesting via bistable systems. *Smart Materials and Structures* 22(2): 023001.

Mann B and Sims N (2009) Energy harvesting from the nonlinear oscillations of magnetic levitation. *Journal of Sound and Vibration* 319(1): 515–530.

Moon FC and Holmes PJ (1979) A magnetoelastic strange attractor. *Journal of Sound and Vibration* 65(2): 275296.

Paradiso J, Starner T et al. (2005) Energy scavenging for mobile and wireless electronics. *Pervasive Computing, IEEE* 4(1): 18–27.

Park C, Walz C and Chopra I (1996) Bending and torsion models of beams with induced-strain actuators. *Smart Materials and Structures* 5(1): 98.

Priya S and Inman DJ (2009) *Energy harvesting technologies*, volume 21. Springer.

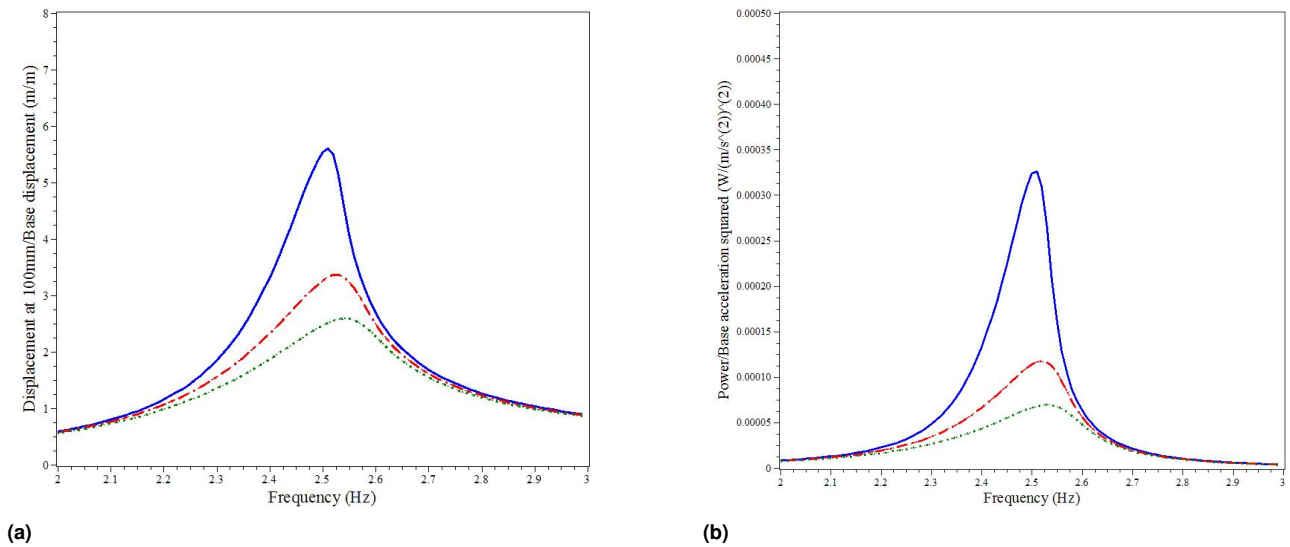


**Figure 8.** The frequency-response curves and the average harvested power for  $M = 0$  g and excitation amplitudes of  $z_0 = 5$  mm (solid), 10 mm (dash-dot), and 15 mm (dashed).

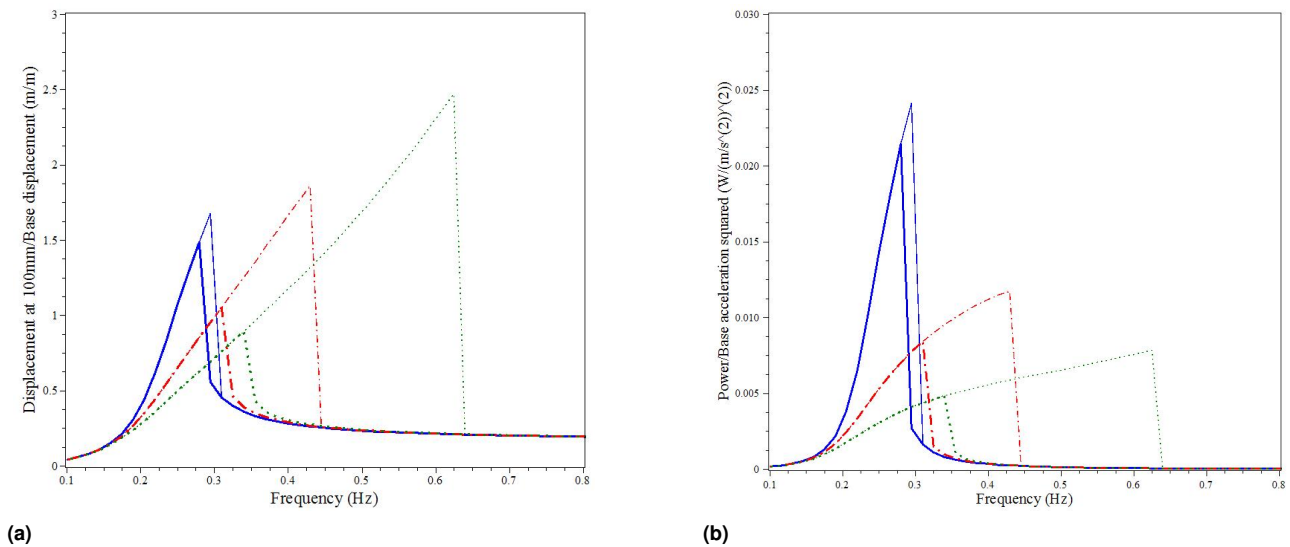


**Figure 9.** The frequency-response curves and the average harvested power for  $M = 10.5$  g and excitation amplitudes of  $z_0 = 5$  mm (solid), 10 mm (dash-dot), and 15 mm (dashed).

Stanton SC, McGehee CC and Mann BP (2009) Reversible hysteresis for broadband magnetopiezoelectric energy harvesting. *Applied Physics Letters* 95(17): 174103.

Xue H, Hu Y and Wang QM (2008) Broadband piezoelectric energy harvesting devices using multiple bimorphs with different operating frequencies. *Ultrasonics, Ferroelectrics, and Frequency Control, IEEE Transactions on* 55(9): 2104–2108.

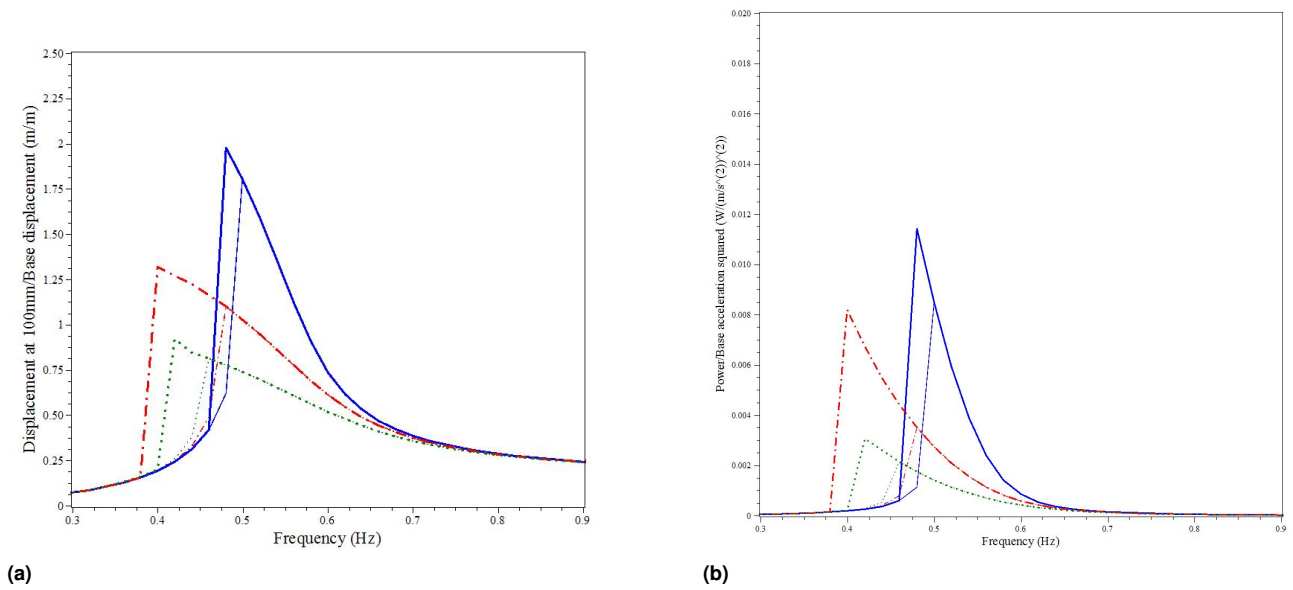


**Figure 10.** The frequency-response curves and the average harvested power for  $M = 14$  g and excitation amplitudes of  $z_0 = 5$  mm (solid), 10 mm (dash-dot), and 15 mm (dashed).